J. Fluid Mech. (2014), *vol.* 738, *pp.* 124–142. © Cambridge University Press 2013
doi:10.1017/jfm.2013.571

Surfactant effect on path instability of a rising bubble

Yoshiyuki Tagawa[1,2,†], **Shu Takagi**[1] **and Yoichiro Matsumoto**[1]

[1]Department of Mechanical Engineering, School of Engineering, The University of Tokyo, 7-3-1 Hongo, Bunkyo-ku, Tokyo 113-8656, Japan

[2]Department of Mechanical Systems Engineering, Tokyo University of Agriculture and Technology, 2-24-16 Nakacho, Koganei-city, Tokyo 184-8588, Japan

(Received 5 January 2013; revised 20 July 2013; accepted 25 October 2013; first published online 4 December 2013)

We report results from the first systematic experiments for investigating surfactant effects on path instability of an air bubble rising in quiescent water. The addition of surfactant to a gas–water system causes a non-uniform distribution of surfactant concentration along the bubble surface, resulting in variations in the gas–water boundary condition from zero shear stress to non-zero shear stress due to the Marangoni effect. This leads to retarded surface velocity and ends up with immobilization of the bubble surface with increasing surfactant concentration, where the drag corresponds to that of a solid sphere of the same size. Using two high-speed cameras and vertical traverse systems, we measure three-dimensional trajectories, velocities and aspect ratios of a millimetre-sized bubble simultaneously for $\sim$1 m. Experimental parameters are the diameter of the bubble and the surfactant concentration of 1-Pentanol or Triton X-100. We explore the surfactant effect on the drag and lift forces acting on the bubble in helical motion. While the drag force monotonically increases with the surfactant concentration as expected, the lift force shows a non-monotonic behaviour. Nevertheless, the direction of the lift force in a reference frame that rotates with the bubble along its trajectory is kept almost constant. We also observe the transient trajectory starting from helical motion to zigzag, which has never been reported in the case of purified water. The instantaneous amplitude and frequency of the transient motion agree with those of the motion regarded as steady. Finally the bubble motions are categorized as straight/helical/zigzag and experimentally examined in the field of two dimensionless numbers: Reynolds number $Re \in [300\ 900]$ and the normalized drag coefficient C_D^* which represents the slip condition. Remarkably it is found that the motions of a bubble with the intermediate slip conditions between free-slip and no-slip are helical for a broad range of Re.

Key words: bubble dynamics, multiphase flow, wakes

1. Introduction

Three-dimensional motions of a millimetre-sized bubble rising in quiescent water is one of the most fascinating and important aspects of bubble hydrodynamics (Ern *et al.* 2012). Typical types of the motions are: a *zigzag* path in which a bubble moves oscillatory in one vertical plane and a *helical* path showing a circular or

† Email address for correspondence: tagawayo@cc.tuat.ac.jp

https://doi.org/10.1017/jfm.2013.571 Published online by Cambridge University Press

an ellipsoidal horizontal motion. This phenomenon is called 'path instability' or 'Leonardo's paradox' (Magnaudet & Eames 2000; Prosperetti *et al.* 2003; Prosperetti 2004; Veldhuis, Biesheuvel & van Wijngaarden 2008), which can be widely seen in nature and industrial processes. It is known that these motions are affected by many factors such as surface-active impurities in water, shape oscillations and wake instabilities. In particular, the presence of impurities often makes it difficult to interpret experimental results, which had prevented the complete understanding of its mechanisms.

For instance, on the one hand, Hartunian & Sears (1957) performed experiments and reported that path instability of a bubble in tap water occurs above the critical Reynolds number $Re_c \sim 202$. On the other hand, Duineveld (1995) reported $Re_c = 662$ in super-purified water. The Re_c of the other observations (e.g. Haberman & Morton 1954; Saffman 1956; Aybers & Tapuku 1969; Tsuge & Hibino 1971; Mercier, Lyrio & Forslund 1997) exist within these values. These discrepancies are owing to the sensitivity of the path instability to surfactant, known as dominant impurities in water.

The main effect of surfactant is to vary a shear stress at the liquid–gas interface as discussed in detail in § 2.2. The effect of surfactant on drag and lift forces acting on a bubble, which rises straight up in water, had been investigated in detail, e.g., by Cuenot, Magnaudet & Spennato (1997), Zhang & Finch (2001) and Fukuta, Takagi & Matsumoto (2008) (for a detailed summary, see the review article by Takagi & Matsumoto (2011)). Jachimska, Warszynski & Malysa (2001) and Krzan & Malysa (2002) investigated the effect of alcohols on the terminal velocity of bubbles. Wang, Papageorgiou & Maldarelli (2002) studied the formation of wakes at order-one Reynolds number for spherical bubbles due to the immobilization of the bubble surface with surfactant. Eggleton, Pawar & Stebe (1999) examined the effects of a monolayer-forming surfactant on a strongly deforming interface. However a systematic exploration of this important parameter on *path instability* is as yet missing.

In this paper we investigate the surfactant effect on path instability of a bubble. To the best of the authors' knowledge, we for the first time perform systematic laboratory experiments and discuss the underlying physical mechanisms. The discussion is based on recent studies for path instability of a bubble with a free-slip condition and a no-slip one, which we briefly summarize below.

Lunde & Perkins (1997), Brücker (2001) and Zenit & Magnaudet (2009) experimentally visualized a wake of a bubble showing path instability: a straight rising bubble has an axisymmetric wake; in helical motion a double-threaded wake (two counter-rotating vorticities) is observed; in zigzag motion a vortex is shed periodically from the wake. de Vries, Biesheuvel & van Wijngaarden (2002) found that the aforementioned phenomena are widely seen in various liquids. These results indicate a significant role of a wake on path instability. Mougin & Magnaudet (2001) carried out direct numerical simulation (DNS) for a bubble as a spheroidal body of fixed shape with a free-slip condition and obtained zigzag and helical paths, consistent with the experimental observations of Ellingsen & Risso (2001). They revealed that one of the origins of the path instability is wake instability. For wake instability of a non-deformable object, slip conditions at the body surface play an important role. Magnaudet & Mougin (2007) investigated the wake instability of a spheroidal object at a fixed position with both a free-slip and a no-slip condition. For the free-slip case, the wake is caused by vorticity accumulation at a rear stagnation point, while for the no-slip case, the separation of the boundary layer originates the wake, as found by Leal (1989). Nevertheless wake dynamics leading to the double-threaded wake or the periodic vortex shedding are similar in nature. Yang & Prosperetti (2007) conducted a

https://doi.org/10.1017/jfm.2013.571 Published online by Cambridge University Press

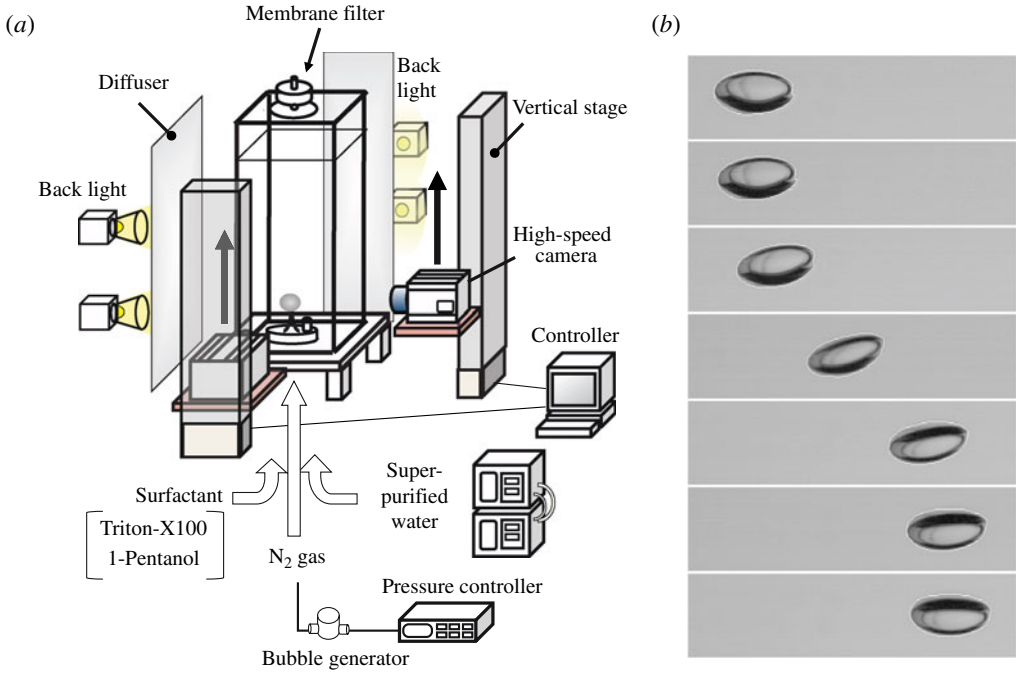


FIGURE 1. (Colour online) (*a*) Experimental system for measuring three-dimensional motions of a bubble. Two cameras attached to vertical traverse stages can trace the bubble for ∼1 m. The super-purified water, surfactant, and nitrogen gas are guided into the tank from the bottom. (*b*) Typical snapshots of a bubble of a diameter $d_e = 2.0$ mm. Time interval of each snapshot is 8 ms.

linear instability analysis for the axisymmetric flow past a fixed-shape spheroid with free-slip boundary conditions. Their results qualitatively resemble those found for the flow past a rigid sphere. These researches indicate the central role of the vorticity on the instability mechanism, independently of its source. Shew & Pinton (2006) and Shew, Poncett & Pinton (2006) measured three-dimensional paths of a bubble rising in super-purified water. They calculated forces acting on a bubble of a free-slip condition using the generalized Kirchhoff equation (Howe 1995; Mougin & Magnaudet 2002).

2. Experimental apparatus and surfactant kinetics

2.1. *Experimental set-up*

Figure 1(*a*) shows a sketch of the experimental set-up.

Considering the fact that impurity of water greatly affects motions of a bubble, we design the set-up with great care for avoiding any impurities as much as possible. We use super-purified water (made by Milli-RX 12α, Milli-Q SP, Millipore co.) as a liquid and Teflon tubes for guiding super-purified water into the tank. The tank is completely closed except an inlet and an outlet for a single bubble. Membrane filters are installed inside the inlet and the outlet to remove any dust larger than 10 μm. We clean the tank using super-purified water at least three times before and after each measurement. For quantifying the purity of the water, total organic carbon (TOC) and electric conductivity of the super-purified water are monitored using the TOC monitor (A-10, Millipore co.) and the electric conductivity meter (SC-82, Yokogawa

https://doi.org/10.1017/jfm.2013.571 Published online by Cambridge University Press

Electric co.). The TOC and the electric conductivity are kept below 20 p.p.b. and over 18.2 MΩ which is comparable with that of the ideal water (18.3 MΩ), respectively.

We design the tank as 10 cm × 10 cm × 100 cm. A distance between a bubble and sidewalls of the tank is more than 10 times larger than the bubble diameter for all experiments. Based on previous investigations summarized by Clift, Grace & Weber (1978), rise velocity for the present condition is estimated below 0.2 % of that in an unbounded quiescent liquid. The temperature of the liquid is in the range of 20–25 °C, measured in each experiment.

We use a nitrogen gas so that dissolution of the gas into the liquid is negligible. A single bubble is generated at the bottom of the test section. Bubble sizes are controlled in the range of 1–4 mm by a bubble generation system which consists of a pressure controller (DPI520, Druck co.), an electric valve, and an audio speaker (F-200, Technics co.). Tomiyama *et al.* (2002) and Wu & Gharib (2002) reported that the methods for introducing a bubble at a bottom of a tank affect the path instability and are categorized into two types: 'large initial shape deformation' and 'small initial shape deformation'. Our study belongs to large deformation type as most of the related work.

For three-dimensional measurements, two digital cameras (MotionPro 10000, Redlake co.) are placed at right angles to each other and attached on vertical traverse systems (KT-45A-B20-100, THK co.) following a bubble vertically for ∼1 m. The frame rate of the cameras is set at 500 frames per second and the shutter speed is at 1 ms. We install telecentric lenses (59LGG950 & 59LGH416, CVI Melles Griot co.) on cameras, providing the same magnification at all object's distances. Figure 1(*b*) shows typical bubble images taken by one of the cameras. The centroid of a bubble and the volume equivalent diameter represent the bubble position and size, respectively. We use a low-pass filter under 60 Hz for the measured path to remove noise due to the vibration of the lenses. Instantaneous frequency f of the oscillation of the bubble horizontal velocity and instantaneous amplitude A of the horizontal projection of the paths are calculated using Hilbert Transform as done by Ellingsen & Risso (2001). We estimate measurement errors of the present system less than 0.1 mm for the position and 2.2 mm s^{-1} for the instantaneous velocity. As an indicator of bubble shape we use the aspect ratio $\chi = a/b$, where a and b are the major and minor axis, respectively.

2.2. *Kinetics of surfactants*

In the presence of surfactant, the distribution of shear stress along the interface is not uniform (e.g. Cuenot *et al.* 1997; Fukuta *et al.* 2008). In the case of high Péclet number Pe ($=d_eU/D$, where d_e is the bubble diameter, U is the bubble velocity and D is the diffusion coefficient), low surfactant concentration compared with the critical micelle concentration (CMC) and low rate constant for desorption, the surfactant on the surface is advected towards the rear part of the bubble, leading to a sudden variation of the surfactant concentration at a given position on the interface. This results in non-uniform distribution of shear stress on the surface, which causes the rear part of the bubble stagnant (Cuenot *et al.* 1997; Fukuta *et al.* 2008). Depending on the position of this jump, the drag coefficient varies between the value corresponding to a clean bubble and a rigid sphere.

In the present study we use 1-Pentanol and Triton X-100 with setting the concentration at 0 p.p.m. (super-purified water) −150 p.p.m. for 1-Pentanol and 0.27 p.p.m. for Triton X-100. The value of the CMC for Triton X-100 is 0.23 mol m^{-3} and the solubility for 1-Pentanol is 2.5×10^3 mol m^{-3}. In our experiment, the concentration for Triton X-100 is 4.4×10^{-4} mol m^{-3}, much lower than the CMC

https://doi.org/10.1017/jfm.2013.571 Published online by Cambridge University Press

and the concentration for 1-Pentanol is up to 1.4 mol m^{-3}. Micelles do not form in the bulk aqueous phase and the drag force is expected to increase with the concentration of surfactant. The Péclet number Pe is of the order of 10^5, i.e. the advection time scale is very small compared with the time scale of the surface diffusion. With this sufficiently high Péclet number the location of the stress jump is dominated by the balance between the advection and adsorption–desorption kinetics of surfactant. The main reason to choose 1-Pentanol and Triton X-100 is that expected experimental observations are very different as described below.

The expected observations in these surfactant solutions rely on the parameters of adsorption and desorption process and surfactant concentrations. The absorption and desorption kinetics on the air–water interface and related constants had been investigated (e.g. Fainerman & Lylyk 1982; Lin, McKeigue & Maldarelli 1990). In a Langmuir framework, an equation for the kinetic rate of surfactant exchange j_s on the air–water interface is

$$j_s = k_a C_s(\Gamma_\infty - \Gamma) - k_d \Gamma, \tag{2.1}$$

where C_s is the sublayer concentration, Γ_∞ is the maximum adsorbed surface concentration, Γ is the surface concentration and k_a and k_d are the rate constants for adsorption and desorption, respectively. The absorption rate k_a of Triton X-100 is $k_a = 50$ m^3 mol^{-1} s^{-1} (Lin *et al.* 1990), approximately 10 times larger than that of 1-Pentanol, $k_a = 5.08$ m^3 mol^{-1} s^{-1}(Fainerman & Lylyk 1982). The values of k_d for Triton X-100 and 1-Pentanol are 3.3×10^{-2} s^{-1} (Lin *et al.* 1990) and 1.10×10^2 s^{-1} (Fainerman & Lylyk 1982), respectively. The equilibrium (or saturated) surface concentration Γ_{max} at $j_s = 0$ is

$$\Gamma_{max} = \frac{k_a C_s}{k_a C_s + k_d} \Gamma_\infty. \tag{2.2}$$

For an initially clean surface ($\Gamma = 0$), the equilibrium surface concentration can be estimated as

$$\Gamma_{max} = \int_0^{\tau_{eq}} j_s(t)\,\mathrm{d}t \sim k_a C_s \Gamma_\infty \tau_{eq}, \tag{2.3}$$

where τ_{eq} is the time required to equilibrate a monolayer on an initially clean surface. Therefore the time τ_{eq} is of the order of $[k_a C_s + k_d]^{-1}$. Using $U_{clean} = 356$ mm s^{-1} for the 2 mm in diameter bubble and the numbers for the rate constants, the distance required to equilibrate a monolayer $z_{eq}/d_e \sim \tau_{eq} U_{clean}/d_e$ is approximately 1.5 for 1-Pentanol solution at 150 p.p.m. and 3000 for the Triton X-100 at 0.27 p.p.m. The bubbles rising in the Triton X-100 solution thus show a slow reduction in velocity. In contrast, in the case of 1-Pentanol, its larger concentration insures a rapid equilibration and the velocity rapidly decelerates.

Using the Gibbs adsorption equation and assuming Langmuir isotherm, the surface equation of state is given by the Szyszkowski equation (2.4) or Frumkin equation (2.5):

$$\sigma = \sigma_0 - R_G T \Gamma_{max} \ln(1 + K_L C_s) \tag{2.4}$$

$$= \sigma_0 + R_G T \Gamma_{max} \ln\left(1 - \frac{\Gamma}{\Gamma_{max}}\right), \tag{2.5}$$

where σ is the surface tension, $\sigma = \sigma_0$ at $\Gamma = 0$, R_G is the perfect gas constant, T is the absolute temperature and K_L is the Langmuir equilibrium adsorption constant.

https://doi.org/10.1017/jfm.2013.571 Published online by Cambridge University Press

The values of Γ_{max} are 2.9×10^{-6} mol m^{-2} and 5.9×10^{-6} mol m^{-2} for Triton X-100 and 1-Pentanol, respectively. The values of K_L are 1.5×10^{3} m^{3} mol^{-1} and 5.6×10^{-3} m^{3} mol^{-1} for Triton X-100 and 1-Pentanol, respectively (Chang & Franses 1995). Equation (2.4) with constants above gives the reduction of the surface tension σ/σ_0 less than 5 % for both surfactants in the range of concentrations used in our experiment. Also, the small reduction in surface tension had been reported: the surface tension is almost unchanged from the clean surface case as measured by Lin *et al.* (1990) for Triton X-100 and by Posner, Anderson & Alexander (1952) for 1-Pentanol for concentrations used in our experiment.

Savic (1953) proposed that the bubble surface could be divided into two different regions separated by a stagnant-cap angle θ_c from the front stagnation point; for $\theta \leqslant \theta_c$ the surface concentration of surfactant Γ is zero and the liquid remains free to slip along the interface, whereas at the rear of the bubble ($\theta \geqslant \theta_c$) Γ is non-zero and the relative tangential velocity vanishes. Sadhal & Johnson (1983) obtained a form of the normalized drag force C_D^* as a function of the cap angle θ in the creeping flow limit and numerical simulations conducted by Fdhila & Duineveld (1996) and Takemura & Yabe (1999) provided strong indications that the hydrodynamical description given by the stagnant-cap model for $Re = O(10^2)$ is realistic to describe the drag. The normalized drag coefficient C_D^* (cf. Cuenot *et al.* 1997) is defined as

$$C_D^* = \frac{C_D - C_{D,clean}}{C_{D,rigid} - C_{D,clean}}, \tag{2.6}$$

where $C_{D,clean}$ and $C_{D,rigid}$ are the drag coefficient of a bubble with a free-slip condition and a no-slip condition, respectively. The free-slip condition and the no-slip condition are thus scaled as $C_D^* = 0$ and 1, respectively. In the present work, we adopt the normalized drag coefficient C_D^* as an indicator of the surface slip condition.

2.3. *Preliminary test: the effect of impurities in super-purified water*

For checking the effect of impurities in super-purified water we measure terminal velocities of bubbles smaller than 1.5 mm in diameter in this set-up. We then obtain the drag coefficient C_D as a function of Reynolds number Re. Here the drag coefficient is calculated by equating the drag to the buoyancy force

$$C_D = \frac{4 d_e g}{3U^2}, \tag{2.7}$$

and the Reynolds number is defined as

$$Re = \frac{U d_e}{\nu}, \tag{2.8}$$

where g is the acceleration of gravity and ν is the kinematic viscosity of a liquid.

The results are shown in figure 2. We also show the drag curves for a sphere with a no-slip condition (Clift *et al.* 1978) and with a free-slip condition (Mei, Klausner & Lawrence 1994). A sphere with a no-slip condition has much larger value of C_D than that with a free-slip condition. The drag curves for a spherical bubble (Mei *et al.* 1994) and theoretical prediction for a deformable bubble (Moore 1965) agree for $Re < 100$ but deviate for $100 < Re$ due to the effect of bubble deformation. The present results are slightly lower than the theoretical curve by Moore (1965) and agree with previous experimental results by Duineveld (1995), Takagi *et al.* (2003) and Sanada *et al.* (2008) in super-purified water. We can thus neglect the impurity of the super-purified water in our set-up. By applying a spatial differential operator along the bubble surface

https://doi.org/10.1017/jfm.2013.571 Published online by Cambridge University Press

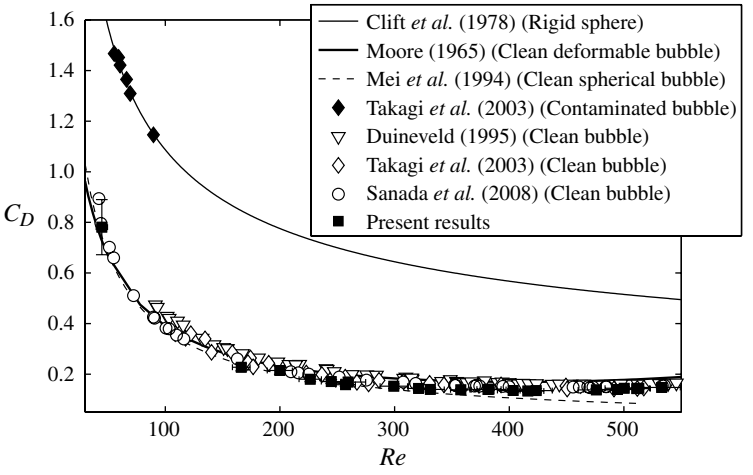


FIGURE 2. Drag coefficient of straight rising bubbles ($d_e < 1.5$ mm): —, an empirical relation for a rigid sphere (Clift *et al.* 1978); —, a model for a clean deformable bubble proposed by Moore (1965); - -, numerical results for a clean spherical bubble by Mei *et al.* (1994); ♦, experimental results for contaminated bubbles by Takagi *et al.* (2003); ▽, experimental results for clean bubbles by Duineveld (1995); ○, experimental results for clean bubbles by Sanada *et al.* (2008); ◇, experimental results for clean bubbles by Takagi *et al.* (2003); ■, present results in super-purified water.

to both sides in (2.5) and appropriate normalization, the Marangoni shear stress on the bubble surface, the origin of the Marangoni effect, can be described as

$$\boldsymbol{n} \times (\boldsymbol{\tau} \cdot \boldsymbol{n}) = -\frac{Ma}{1-\Gamma} \nabla_s \Gamma, \tag{2.9}$$

where $\boldsymbol{n}$ is the unit normal vector on the surface, ∇_s is a spatial differential operator along the bubble surface and ρ is the density of the liquid. Here Ma is the Marangoni number,

$$Ma = \frac{R_G T \Gamma_{max}}{\rho \nu U}. \tag{2.10}$$

We recall that in the present condition the Péclet number is so high that the location of the stress jump is dominated by the balance between the advection and adsorption–desorption kinetics of surfactant. In this case, equation (2.9) shows that the Marangoni number determines the strength of the Marangoni shear stress that causes the drag. With increasing bubble size at the same surfactant solution, the Marangoni number decreases owing to an increase of rise velocity U. Thus, in general, the effect of surfactant on the drag coefficient decreases with the bubble size. The present study investigates a bubble of $d_e > 1.5$ mm, larger than those presented in figure 2. The effect of impurity is therefore even smaller.

3. Results and discussion

In this section we show results for studying the effect of 1-Pentanol on path instability in § 3.1. In the latter part of this section we investigate the relation between the slip condition and forces acting on a bubble. In § 3.2 we analyse a transient motion of a bubble due to the effect of Triton X-100. In § 3.3 we provide a phase diagram

https://doi.org/10.1017/jfm.2013.571 Published online by Cambridge University Press

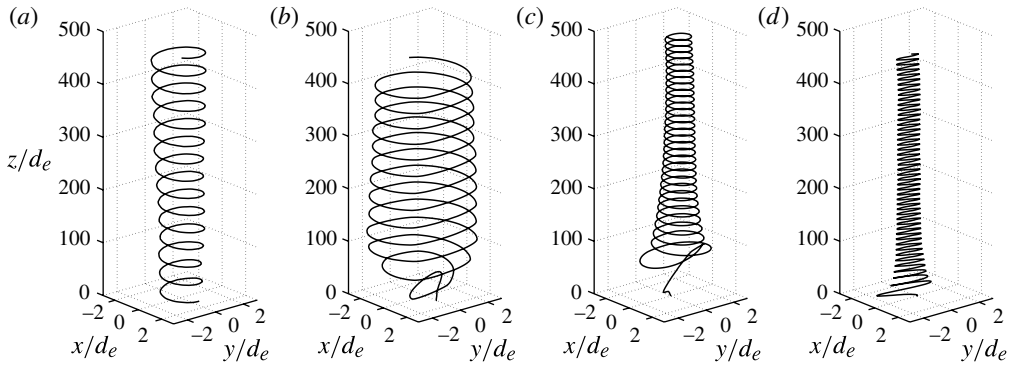


FIGURE 3. Trajectories of a bubble ($d_e = 2.0 \pm 0.1$ m min) in 1-Pentanol solution for (*a*) 0 p.p.m. (super-purified water), (*b*) 25 p.p.m., (*c*) 75 p.p.m. and (*d*) 150 p.p.m. The helical motions are seen in the 1-Pentanol solution for lower concentration (*a–c*) while the zigzag motions are observed for higher concentration (*d*).

using the Reynolds number Re and the slip condition represented by C_D^*, defined at (2.6) in order to examine the ranges of parameters for obtaining straight/helical/zigzag motions.

3.1. *Surfactant effect on quasi-steady motion*

Figure 3 shows typical trajectories of a bubble in 1-Pentanol solution at different concentration. The size of the bubbles d_e is 2.0 ± 0.1 mm, which have no shape oscillation in filtered tap water in which contamination does not have a significant effect on the bubble motion in the considered experimental conditions (Ellingsen & Risso 2001). These three-dimensional motions clearly show a dependence on surfactant concentration. We observe helical trajectories in super-purified water (figure 3*a*) and in 1-Pentanol solution in the cases of lower concentration (figure 3*b,c*). The zigzag motions are found in higher concentration (figure 3*d*). Tsuge & Hibino (1971) found an empirical relation for path instability of a rising bubble in a stationary liquid:

$$St = fd_e/U = 0.100C_D^{0.734}, \tag{3.1}$$

where St is the Strouhal number and f is the frequency of the bubble horizontal velocity. This relation is satisfied within 30 % in both purified water and surfactant solutions. Our measurements are within 30 % of the empirical relation (3.1). Figure 4 shows rise velocities U corresponding to the trajectories presented in figure 3. The bubble in the super-purified water has the fastest velocity $U_{clean} = 356 \pm 4$ mm s^{-1}, which agrees with the result of Duineveld (1995), $U_{clean} = 354$ mm s^{-1}. In the surfactant solution bubbles first accelerate in the low z/d_e region and then decelerate. For higher position $z/d_e > 300$ the velocity approaches the terminal velocity, which decreases with increasing surfactant concentration. This tendency is the same as that for straight rising bubbles (cf. Frumkin & Levich 1947; Fdhila & Duineveld 1996; Liao & McLaughlin 2000; Takagi *et al.* 2003). This indicates that the slip conditions are varied by the concentration of 1-Pentanol solution. For a zigzagging bubble in surfactant solution of 150 p.p.m. the vertical velocity shows oscillations. The frequency of the vertical velocity f_v is 17.9 Hz, which is twice as large as that of the horizontal velocity, $f = 8.93$ Hz. It is found experimentally by de Vries *et al.*

https://doi.org/10.1017/jfm.2013.571 Published online by Cambridge University Press

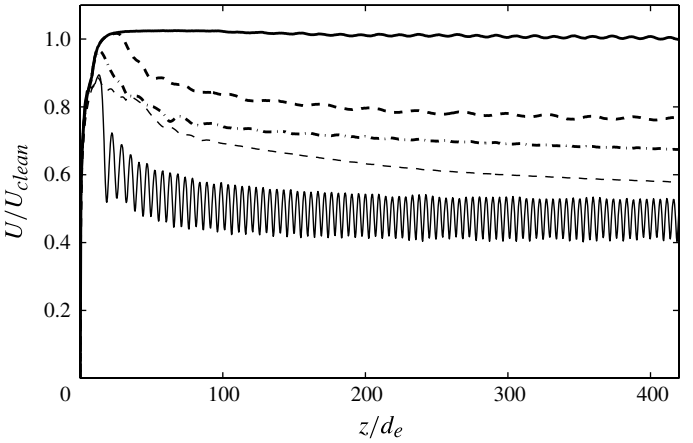


FIGURE 4. The rise velocity U as a function of the vertical position of a bubble (z) normalized by the bubble diameter (d_e). The thick line is the bubble velocity in 0 p.p.m. 1-Pentanol solution (super-purified water), the thick dashed line in 25 p.p.m. solution, the thick dashed–dotted line in 75 p.p.m., the thick dashed line in 100 p.p.m. and the thin line in 150 p.p.m. The lines for 0, 25, 75 and 150 p.p.m. correspond to the trajectories of (a–d) in figure 3, respectively.

(2002) and numerically by Mougin & Magnaudet (2006) that zigzagging bubbles have a double-threaded wake of which the axially vorticity components switch sign twice in one period of zigzag. This would be the reason why the frequency of the bubble's vertical velocity is twice that of its horizontal velocity. In addition, it is interesting to note that the frequency of the vortex shedding from the rear part of a rigid sphere is (Kim & Pearlstein 1990)

$$f_v = \frac{\omega v Re}{\pi d_e^2}, \tag{3.2}$$

where ω is 0.30. We obtain $\omega = 0.30 \pm 0.02$ for a zigzagging bubble in surfactant solution of 150 p.p.m., which has a spherical shape and the drag coefficient close to a rigid sphere as shown later. This indicates that the mechanism of the vorticity generation and the periodic vortex shedding for the high-concentration case is similar to that of a rigid sphere, where the frequency of the vortex shedding is defined by the stable position of the vortex column (Saffman 1992).

For a straight rising bubble it becomes more spherical with increasing C_D^*: for higher C_D^* the rise velocity is lower, resulting in lower Weber number,

$$We = \frac{\rho U^2 d_e}{\sigma}, \tag{3.3}$$

where σ is the surface tension. Thus, the surface tension plays a dominant role, leading to the spherical shape. Recall that the decrease of the surface tension at the bubble surface due to the absorption of surfactant is less than 5 % as discussed in § 2.2. Figure 5(a) shows the aspect ratio χ of bubbles in three-dimensional motion as a function of the normalized slip condition C_D^*. The shape of the bubble is more spherical with the slip condition being closer to no-slip. This trend is consistent with that for a straight rising bubble. Zenit & Magnaudet (2008) revealed that the criterion

https://doi.org/10.1017/jfm.2013.571 Published online by Cambridge University Press

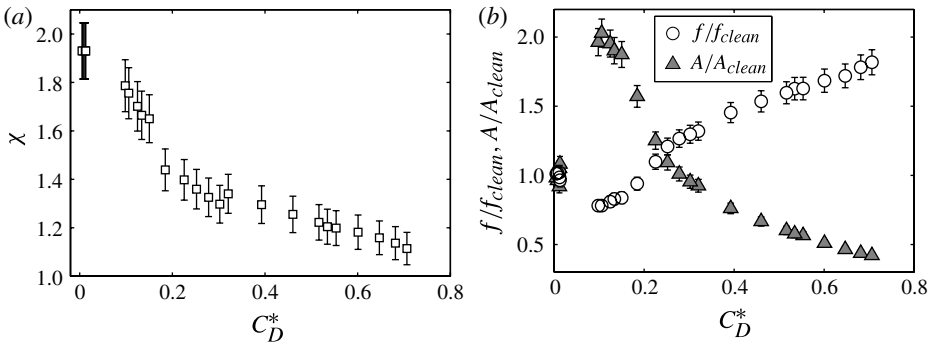


FIGURE 5. (*a*) The aspect ratio χ as a function of the normalized slip condition C_D^*. (*b*) The frequency f of the bubble horizontal velocity (◯) and the amplitude A of the bubble horizontal trajectory (△) as a function of the normalized slip condition C_D^*.

of path instability of a bubble with a free-slip surface is not the Reynolds number but the aspect ratio $\chi \geqslant 2.0$ of the bubble shape. The aspect ratio of a bubble with a free-slip condition in figure 5(*a*) is $\chi \approx 2.0$, satisfying the criterion. In contrast, for higher C_D^*, the χ is below the criterion, suggesting the effect of surfactant that triggers path instability.

The bubble trajectory projected on a horizontal plane is represented by the frequency f and the amplitude A as shown in figure 5(*b*). With increasing C_D^* the amplitude A first increases, reaching the maximum, and then decreases. The variation of A is large, as the maximum A is about five times larger than the minimum A. The frequency f first decreases, reaching a minimum, and then increases. These non-monotonic dependencies on C_D^* should reflect the nature of the underlying physical mechanisms, i.e. forces acting on a bubble, which we shall discuss in the following.

For the shape oscillation Duineveld (1995) found that the shape oscillation starts at $We > 5$ and Lunde & Perkins (1997) observed the shape oscillation with the bubble diameter (d_e) being larger than 3.5 mm. These parameters for the present experiments are $We < 5$ and $d_e < 3.5$ mm. Furthermore, we measure the bubble shapes for four periods at (*a*) $C_D^* = 0$ and (*b*) $C_D^* = 0.4$ above $z/d_e > 300$ shown in figure 6. The amplitude of the shape oscillation is less than 0.024 mm, which is in the order of the measurement error, suggesting that the shape oscillation is negligible.

For a non-deformable body moving freely in viscous flow, the generalized Kirchhoff equation (Howe 1995; Mougin & Magnaudet 2002) can be used. In addition, if the symmetry axis of the ellipsoidal bubble is aligned with the bubble velocity vector, the generalized Kirchhoff equation reduces to (cf. Shew *et al.* 2006)

$$\boldsymbol{F} = \begin{bmatrix} F_1 \\ F_2 \\ F_3 \end{bmatrix} = \begin{bmatrix} -F_{B1} \\ -F_{B2} \\ -(\mathrm{d}\phi/\mathrm{d}t)A_{11}U\sin\theta \end{bmatrix}, \tag{3.4}$$

where

$$A_{11} = \rho V \frac{(\chi-1)^{1/2} - \cos^{-1}\chi^{-1}}{\cos^{-1}\chi^{-1} - (\chi^2-1)^{1/2}/\chi^2}. \tag{3.5}$$

https://doi.org/10.1017/jfm.2013.571 Published online by Cambridge University Press

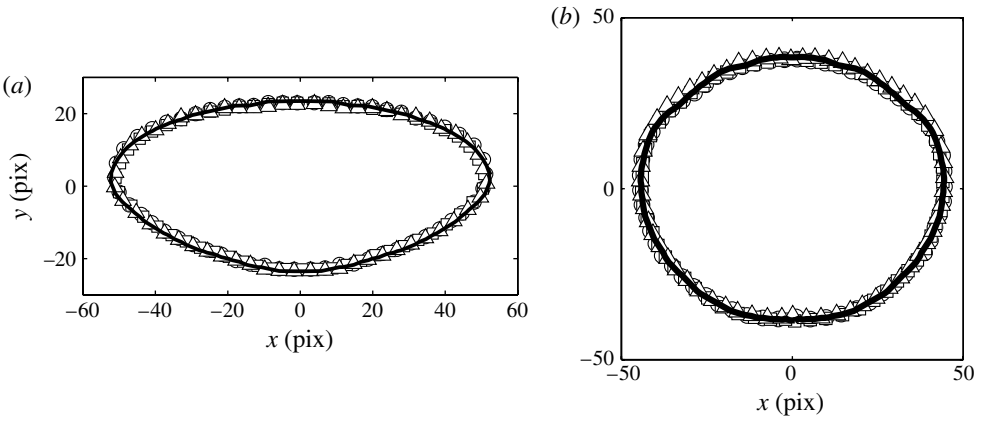


FIGURE 6. The bubble shape at (*a*) $C_D^* = 0$ and (*b*) $C_D^* = 0.4$ for four periods of helical paths (△, ◯, □, —). The shape change is less than 0.024 mm, implying that the shape change is negligible.

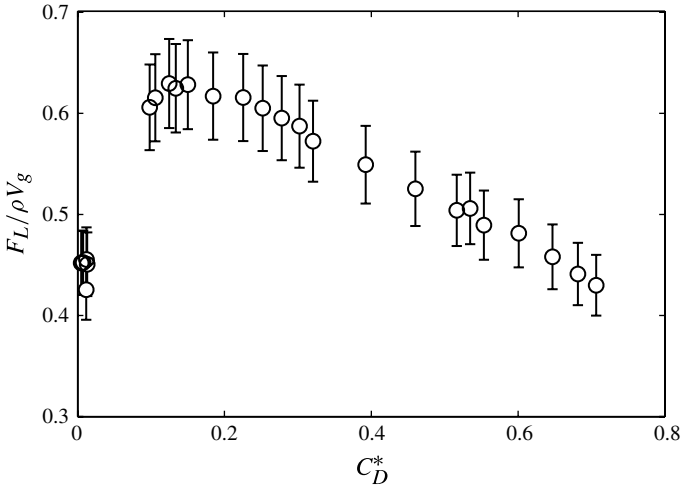


FIGURE 7. The magnitude of the lift force F_L acting on the bubble as a function of the normalized slip condition C_D^*. The lift force show non-monotonic dependence on the slip condition. The maximum lift force is found around $C_D^* = 0.12$, corresponding to the maximum amplitude A and the minimum frequency f.

Here θ is the pitch angle of the path and ϕ is the azimuthal angle against the direction of motion. The subscripts 1, 2 and 3 indicate the components of the forces in directions 1, 2 and 3, respectively. Direction 1 is the same direction as the minor axis of a bubble, direction 2 is taken as the plane 1–2 being vertical and direction 3 is normal to the plane 1–2 with setting the right-hand coordinate. The origin of these Cartesian coordinates (1, 2, 3) is the centroid of the bubble. Here F_{B1} and F_{B2} are the components of the buoyancy force in directions 1 and 2, respectively.

The magnitude of lift force $F_L = \sqrt{F_2^2 + F_3^2}$ calculated by (3.4) is shown in figure 7. Remarkably the lift force shows a non-monotonic dependence on the slip condition.

https://doi.org/10.1017/jfm.2013.571 Published online by Cambridge University Press

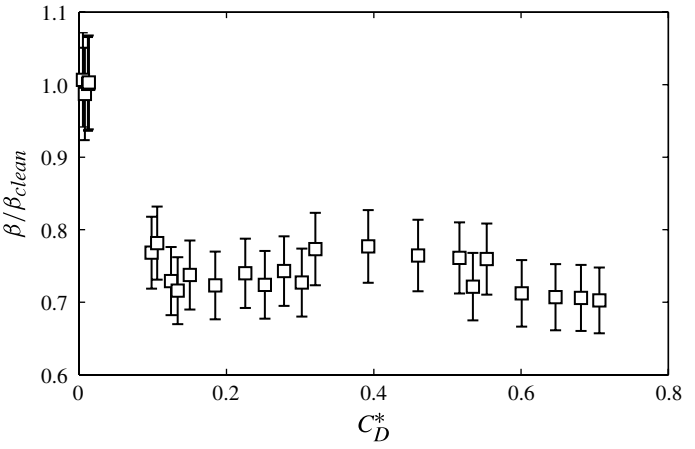


FIGURE 8. The angle of the lift force β in the reference frame as a function of C_D^* normalized by $\beta_{clean} = 0.92$ rad at $C_D^* = 0$. Remarkably, β is almost constant in $C_D^* > 0$ and lower than that in $C_D^* = 0$. This indicates that the direction of the lift force is constant in the surfactant solution for the bubble of $d_e = 2.0$ mm.

The maximum lift force is found around $C_D^* = 0.12$, corresponding to the maximum amplitude A and the minimum frequency f. de Vries *et al.* (2002) estimated the magnitude of the lift force as

$$F_L = \rho\gamma l U, \tag{3.6}$$

where γ is the circulation of the vortex in the direction of motion and l is the distance between the treads of double wakes. For the present case this estimation gives the order of the lift force, 20–40 μN, in good agreement with experiments, 20–30 μN. Based on (3.6) one possible mechanism for the non-monotonic behaviour of the lift force is as follows: for the $C_D^* < 0.12$ the vortex generation sharply increases with increasing C_D^*, resulting in the increase of the circulation γ. This effect exceeds the effect of decreasing the rise velocity U, leading to the increase of the lift force. In contrast, for $C_D^* > 0.12$, the increase rate of γ is less than the decrease of U, resulting in the decrease of the lift force.

In figure 8 we show an angle of the lift force β in the reference frame normalized by $\beta_{clean} = 0.92$ rad at $C_D^* = 0$. Remarkably the β is almost constant for non-zero C_D^*. Brücker (2001) and Zenit & Magnaudet (2009) showed that the direction of the lift force is on the symmetric plane of the double-threaded wake. Thus, the constant β indicates that the alignment of double-threaded wake in the reference frame is independent of the slip condition for $C_D^* > 0$. Note that the value of this constant β is lower than that at $C_D^* = 0$, indicating that the symmetric plane of the double-threaded wake for $C_D^* > 0$ is closer to the direction of motion of a bubble. The reason for this is not clear at the moment. One possible reason is that for $C_D^* > 0$ the rear part of the bubble surface has high surface concentration of surfactant that provides the similar boundary condition in the azimuthal direction.

3.2. *Surfactant effect on transient motion*

We observe transient trajectories of a bubble in Triton X-100 solution: figure 9(*a–c*) show straight–helical–zigzag transition for a bubble of 1.3 mm in diameter, helical–zigzag for a bubble of 2.0 mm and zigzag–helical–zigzag for a bubble of

https://doi.org/10.1017/jfm.2013.571 Published online by Cambridge University Press

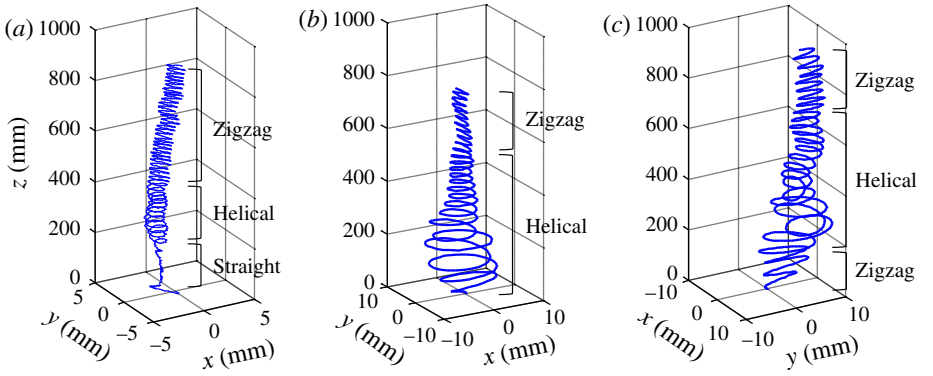


FIGURE 9. (Colour online) The three-dimensional trajectories of rising bubbles in Triton X-100 solution: (*a*) a bubble of 1.3 mm in diameter first rises straight, then changes into a helical motion, followed by a zigzag motion; (*b*) a bubble of 2.0 mm in diameter demonstrates the transient trajectory changing from a helical into a zigzag motion; (*c*) a bubble of 3.1 mm in diameter shows a zigzag–helical–zigzag transition.

3.1 mm. In the following we discuss the transient trajectory of a bubble of 2.0 mm in diameter in comparison with quasi-steady trajectories as reported in § 3.1.

The helical–zigzag transition shown in figure 9(*b*) has never been reported while the opposite transition, zigzag–helical transition, is found for a bubble with a free-slip condition in both experiments (e.g. Shew *et al.* 2006) and numerics (e.g. Mougin & Magnaudet 2001). A comprehensive description for zigzag–helix transition is given by Mougin & Magnaudet (2006): a planar symmetry of the double-treaded wake which drives the zigzag motion is broken and the two vortices wrap around each other, allowing the trajectory to become three-dimensional, i.e. helical. In this case the helical–zigzag transition has not be seen. For the present experiments, therefore, another mechanism should be dominant, which we discuss below.

For studying this mechanism further the corresponding rise velocity of figure 9(*b*) is shown in figure 10. It first approaches the velocity of a bubble with a free-slip condition, then decreases continuously and finally comes close to that of a bubble for a no-slip condition with velocity oscillations. This reduction of the velocity shows that the slip condition gradually changes from free-slip to no-slip for a long distance $\sim$1 m. This is attributed to the continuous accumulation of Triton X-100 on the bubble surface as discussed in § 2.2, resulting in the gradual increase of drag. A similar trend of this velocity decrease had been reported by Zhang & Finch (2001) for smaller bubbles rising straightly in a quiescent liquid. This extended reduction in velocity allows us to observe the transition from helical to zigzag. The three-dimensional motion is helical for $z/d_e \leqslant 290$ where the velocity of the bubble is higher than the transition velocity $U_c/U_{clean} = 0.55$, corresponding to the slip condition of $C_D^* < 0.7$. For $z/d_e > 290$ the bubble motion is zigzag with mean velocity lower than U_c and the velocity shows oscillation. This suggests that the transient slip condition dominates the transient motion of a bubble. In addition, the transition velocity U_c is the same as that for quasi-steady motion in 1-Pentanol. This indicates that the *instantaneous* slip condition of the bubble in this transient motion could be considered as the slip condition which leads to the corresponding quasi-steady path instability as shown in § 3.1. The reason why the quasi-steady assumption works well is not clear at this moment. The total time for developing a wake from a moment when a bubble starts

https://doi.org/10.1017/jfm.2013.571 Published online by Cambridge University Press

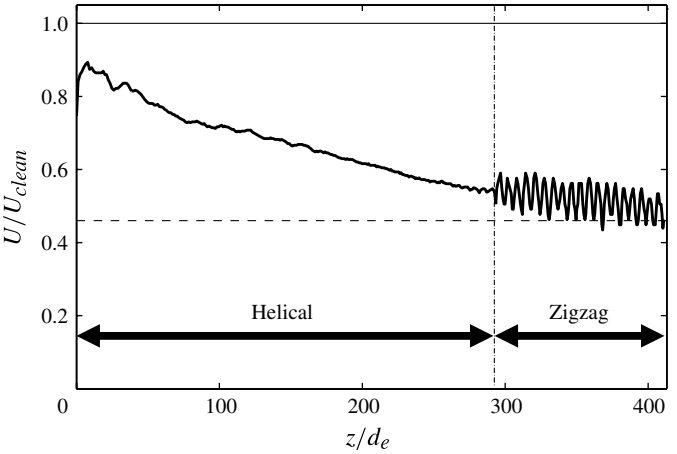


FIGURE 10. The rise velocity U in Triton X-100 0.27 p.p.m. solution as a function of the bubble vertical position z. The vertical and lateral axis are represented by the unit of U_{clean} and d_e, respectively. The thin solid line is the velocity of a bubble with a free-slip condition and thin dashed line is that of a bubble with a no-slip condition. For $z/d_e \leqslant 290$ ($U/U_{clean} = 0.55$) the bubble motion is helical while for $z/d_e > 290$ the bubble motion is zigzag.

moving at constant speed is estimated as the vorticity diffusion time scale, w^2/ν, where ν is the kinematic viscosity and w is the semiwidth of the wake. In our condition it is in the order of 1 s, in the same order of total time for changing surface condition ∼5 s. We here propose one hypothesis. Mougin & Magnaudet (2006) found that there is a time delay $\sim 5d_e/U$ between the change of sign of the trailing vortices and the vanishing of the body rotational velocity at the inflection points of the zigzag path. It may show that the length of the wake which affects the bubble motion is $\sim 5d_e$. Adding the vorticity advection time scale with the time delay between the change inside the wake and bubble velocity may give the time $\sim 10d_e/U \sim O(0.1)$ s, much smaller than the time for changing surface condition.

For validating this interpretation, we investigate the relationship between the instantaneous slip condition C_D^* and the amplitude A of the bubble trajectory projected on a horizontal plane (see figure 11). The non-monotonic dependence on the C_D^* is again observed as discussed in § 3.1. In figure 11 we also show the measurements for quasi-steady motion. Remarkably the results for both cases agree within measurement errors, which could support the interpretation.

3.3. *Phase diagram of the surfactant effect on a single-bubble path instability*

In this subsection we discuss the range of parameters for obtaining the typical types of motions: straight, helical and zigzag. The parameters are the Reynolds number (Re) and the slip condition represented by the normalized drag coefficient (C_D^*). In figure 12, the types of path instability regarded as quasi-steady motion are plotted in the Re–C_D^* space. This is the first mapping of bubble behaviours for a wide range of the slip conditions and the Reynolds numbers.

The results of a bubble with both a free-slip and a no-slip condition show a consistent trend with previous investigations, exhibiting a clear dependence on Re (e.g. Duineveld 1995; Ellingsen & Risso 2001; Shew *et al.* 2006 for a free-slip condition and Fdhila & Duineveld 1996; Jenny, Dusek & Bouchet 2004 for a no-slip

https://doi.org/10.1017/jfm.2013.571 Published online by Cambridge University Press

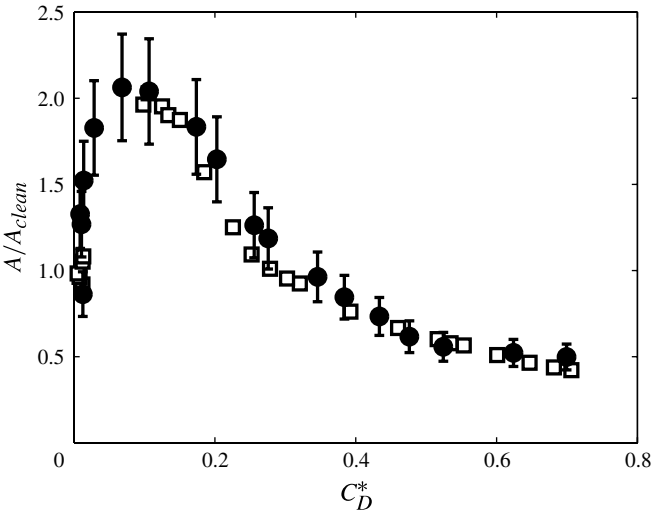


FIGURE 11. The amplitude A of the horizontal trajectory for the bubble of the transient motion (filled circles) and that of quasi-steady motion (open squares) as a function of the normalized drag coefficient C_D^*. The measured amplitudes are normalized by the amplitude of a bubble with a free-slip condition A_{clean}. The results of the transient motion show an agreement with that of the quasi-steady motion, indicating that the instantaneous slip condition can be regarded as the quasi-steady slip condition which leads to the corresponding path instability as shown in § 3.1.

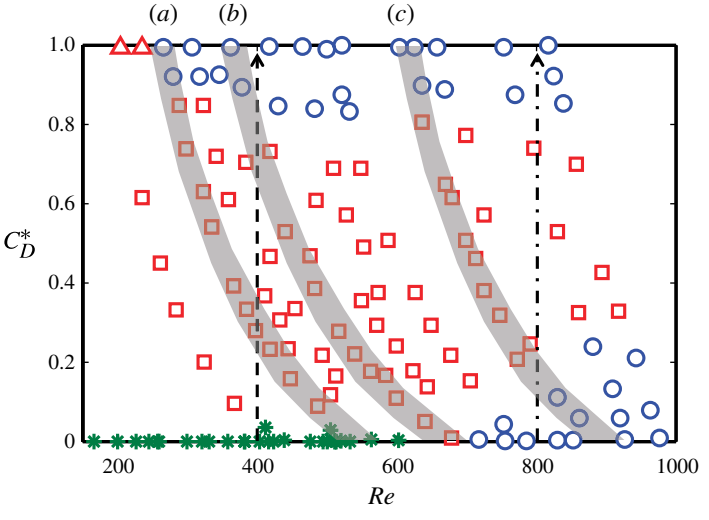


FIGURE 12. (Colour online) The parameter field of Reynolds number Re and the slip condition represented by the normalized drag coefficient C_D^*: asterisk, straight rising motion; square, helical motion; triangle, oblique motion; circle, zigzag motion. The grey regions of (a–c) indicate the bubble trajectories for (a–c) in figure 9, respectively.

condition): a bubble with a free-slip condition, indicated by the line of $C_D^* = 0$ in figure 12 rises straightly for $Re < 600$; for $Re \sim 650$ a bubble demonstrates helical motion; for $Re > 700$ a bubble shows zigzag motion. Bubbles which do not exhibit

https://doi.org/10.1017/jfm.2013.571 Published online by Cambridge University Press

path instability with free-slip surfaces at $C_D^* = 0$ have the aspect ratio less than 2.0, consistent with the results of Zenit & Magnaudet (2008). The behaviours of a bubble with a no-slip condition, along $C_D^* = 1$ in figure 12, show a good agreement with the existing results of a rigid sphere; the oblique motion is observed for $210 < Re < 270$ and the zigzag motion for larger Re regime. Note that the helical motion is never seen in this region. As discussed by Fdhila & Duineveld (1996), Magnaudet & Mougin (2007) and Yang & Prosperetti (2007), the path instability of a bubble with a no-slip condition has a similar mechanism as that of a rigid sphere.

With the intermediate slip condition for $0.4 < C_D^* < 0.6$, in contrast, a bubble shows helical motions for an entire range of the Reynolds number in this study, i.e. $Re \in [300, 900]$.

To understand this phase diagram, we first discuss the behaviour of a bubble with a free-slip and a no-slip condition. The flow evolution with an object with a fixed spheroidal shape ($\chi = 2.5$) is studied by Magnaudet & Mougin (2007). With increasing the maximum vorticity by increasing the Reynolds number, the flow first undergoes a supercritical *regular* bifurcation which leads to a steady double-threaded wake with a planar symmetry. This is strongly related to the oblique motion for a freely moving bubble with a no-slip condition and the helical motion for a free-slip condition. By further increasing the Reynolds number, a secondary supercritical *Hopf* bifurcation occurs. The sign of the streamwise vorticity shed in each thread changes periodically. This is quite relevant to the zigzag motion of a freely moving bubble with both a free-slip and a no-slip condition. We find that the aforementioned mechanism nicely explain their dependence on the Reynolds numbers of a bubble with a free-slip and a no-slip condition.

We now view this phase diagram with varying C_D^* at fixed Re in the region of $Re < 600$ (cf. the dashed arrow for $Re = 400$ in figure 12). Note that with increasing C_D^* at fixed Re the total vorticity generation at the bubble surface increases. With increasing C_D^* at $Re < 600$ bubble motion first changes from straight to helical and then helical to zigzag. It indicates that the enhancement of the vorticity generation due to the changing of the slip condition first leads to the regular bifurcation for the helical motions and then the Hopf bifurcation for the zigzag motions. This is the same way of evolution of the flow bifurcation for a free-slip and a no-slip bubble with varying Re as described in the previous paragraph. With increasing C_D^* at fixed $Re > 700$ (cf. the dashed–dotted arrow for $Re = 800$ in figure 12), however, the bubble motion first shows zigzag, followed by helical and then comes back to the zigzag motion. This transition is clearly different from that for $Re < 600$. The possible reason could be given by the maximum local vorticity generated on the bubble surface. A bubble with a free-slip condition shows a larger deformation, which gives a larger local curvature and leads to higher local vorticity generated on the bubble surface (Batchelor 1967). This high local vorticity could trigger the vortex shedding from the bubble surface. For a bubble with an intermediate slip condition, the moderate deformation generates moderate local vorticity which may be smaller than that with a free-slip condition. For a bubble with a no-slip condition, the immobile surface generates larger local vorticity which could again trigger the periodic vortex shedding. To address this point, further experiments and numerics are required.

4. Conclusion

In this work we have experimentally investigated surfactant effects on the path instability of a single bubble rising in quiescent liquid and discussed the underlying

https://doi.org/10.1017/jfm.2013.571 Published online by Cambridge University Press

mechanisms. We have obtained three-dimensional trajectories, velocities and aspect ratios of the bubble for $\sim$1 m using two high-speed cameras and vertical traverse systems. We have controlled the diameter of the bubble in the range of 1–4 mm and the surfactant concentration of 1-Pentanol or Triton X-100. The addition of surfactant has varied the surface slip condition from a free-slip to a no-slip condition due to Marangoni effect. The slip condition have been quantified using the normalized drag coefficient C_D^* which is the experimental drag coefficient scaled by the drag coefficients of a free-slip and a no-slip condition. We have first shown the effect of 1-Pentanol on the path instability. The three-dimensional motion has been changed drastically with varying surfactant concentration. We have explored the relationship between the slip condition and the forces acting on the bubble. Remarkably, the lift force has shown a non-monotonic dependence on the slip condition, although the direction of the lift force has been constant in the reference frame. It implies that the double-threaded wake has the fixed alignment of the vortices. We have also observed the transient trajectory starting from helical to zigzag, which has never been reported before. Its instantaneous frequency of the bubble horizontal velocity and amplitude of the horizontal path have agreed with those of quasi-steady motions, indicating that the wake can follow the time evolution of the slip condition in a very short time for this case. Finally we have investigated the parameter range for obtaining straight/helical/zigzag motion in the Re–C_D^* space. While types of bubble motions have been strongly dependent on Re in the case of a free-slip and a no-slip condition, those in intermediate slip conditions for $0.4 < C_D^* < 0.6$ have been helical for the broad range of $Re \in [300, 900]$.

Acknowledgements

We thank W. Kawaguchi and A. Funakubo for helping the experiments. Y.T. thanks for financial support from Grant-in-Aid for JSPS Fellows (grant number 20-10701). We also thank for Grant-in-Aid for Scientific Research (B) (grant number 21360079). We appreciate F. Takemura, K. Sugiyama, T. Ogasawara, A. Prosperetti, L. van Wijngaarden and D. Lohse for fruitful discussions. We also thank all of the reviewers for their constructive comments and suggestions.

REFERENCES

AYBERS, N. M. & TAPUKU, A. 1969 The motion of gas bubbles rising through a stagnant liquid. *Wärme-Stoffübertrag* **2**, 118–128.

BATCHELOR, G. K. 1967 *An Introduction to Fluid Dynamics*. Cambridge University Press.

BRÜCKER, C. 2001 Spatio-temporal reconstruction of vortex dynamics in axisymmetric wakes. *J. Fluid Struct.* **15**, 543–554.

CHANG, C. H. & FRANSES, E. I. 1995 Adsorption dynamics of surfactants at the air/water interface: a critical review of mathematical models, data, and mechanisms. *Colloids Surf.* A: *Physicochem. Eng. Aspects* **100**, 1–45.

CLIFT, R., GRACE, J. R. & WEBER, M. E. 1978 *Bubbles, Drops and Particles*. Academic Press.

CUENOT, B., MAGNAUDET, J. & SPENNATO, B. 1997 The effects of slightly soluble surfactants on the flow around a spherical bubble. *J. Fluid Mech.* **339**, 25–53.

DUINEVELD, P. C. 1995 The rise velocity and shape of bubbles in pure water at high Reynolds number. *J. Fluid Mech.* **292**, 325–332.

EGGLETON, C. D., PAWAR, Y. P. & STEBE, K. J. 1999 Insoluble surfactants on a drop in an extensional flow: a generalization of the stagnated surface limit to deforming interfaces. *J. Fluid Mech.* **385**, 79–99.

https://doi.org/10.1017/jfm.2013.571 Published online by Cambridge University Press

ELLINGSEN, K. & RISSO, F. 2001 On the rise of an ellipsoidal bubble in water: oscillatory paths and liquid-induced velocity. *J. Fluid Mech.* **440**, 235–268.

ERN, P., RISSO, F., FABRE, D. & MAGNAUDET, J. 2012 Wake-induced oscillatory paths of bodies freely rising or falling in fluids. *Annu. Rev. Fluid Mech.* **44** (1), 97–121.

FAINERMAN, V. B. & LYLYK, S. V. 1982 Dynamic surface tension and kinetics of adsorption in solutions of normal alcohols. *Kolloidn. Z.* **44**, 538–544.

FDHILA, R. B. & DUINEVELD, P. C. 1996 The effect of surfactant on the rise of a spherical bubble at high Reynolds and Péclet numbers. *Phys. Fluids* **8**, 310–321.

FRUMKIN, A. & LEVICH, V. G. 1947 On surfactants and interfacial motion. *Zh. Fiz. Khim.* **21**, 1183–1204.

FUKUTA, M., TAKAGI, S. & MATSUMOTO, Y. 2008 Numerical study on the shear-induced lift force acting on a spherical bubble in aqueous surfactant solutions. *Phys. Fluids* **20**, 040704.

HABERMAN, W. L. & MORTON, R. K. 1954 An experimental study of bubbles moving in liquids. *Trans. ASCE* **387**, 227–252.

HARTUNIAN, R. A. & SEARS, W. R. 1957 On the instability of small gas bubbles moving uniformly in various liquids. *J. Fluid Mech.* **3** (01), 27–47.

HOWE, M. S. 1995 On the force and moment on a body in an incompressible fluid, with application to rigid bodies and bubbles at high and low Reynolds numbers. *Q. J. Mech. Appl. Maths* **48**, 401–426.

JACHIMSKA, B., WARSZYNSKI, P. & MALYSA, K. 2001 Influence of adsorption kinetics and bubble motion on stability of the foam films formed at *n*-octanol, *n*-hexanol and *n*-butanol solution surface. *Colloids Surf.* A: *Physicochem. Eng. Aspects* **192** (1), 177–193.

JENNY, M., DUSEK, J. & BOUCHET, G. 2004 Instabilities and transition of a sphere falling or ascending freely in a Newtonian fluid. *J. Fluid Mech.* **508**, 201–239.

KIM, I. & PEARLSTEIN, A. J. 1990 Stability of the flow past a sphere. *J. Fluid Mech.* **211**, 73–93.

KRZAN, M. & MALYSA, K. 2002 Profiles of local velocities of bubbles in *n*-butanol, *n*-hexanol and *n*-nonanol solutions. *Colloids Surf.* A: *Physicochem. Eng. Aspects* **207** (1), 279–291.

LEAL, L. G. 1989 Vorticity transport and wake structure for bluff bodies at finite Reynolds number. *Phys. Fluids* A: *Fluid Dyn.* **1**, 124–131.

LIAO, Y. & MCLAUGHLIN, J. B. 2000 Bubble motion in aqueous surfactant solutions. *J. Colloid Interface Sci.* **224** (2), 297–310.

LIN, S. Y., MCKEIGUE, K. & MALDARELLI, C. 1990 Diffusion-controlled surfactant adsorption studied by pendant drop digitization. *AIChE J.* **36** (12), 1785–1795.

LUNDE, K. & PERKINS, R. J. 1997 Observations on wakes behind spheroidal bubbles and particles. In *1997 ASME Fluids Engineering Division Summer Meeting*, pp. 1–8.

MAGNAUDET, J. & EAMES, I. 2000 The motion of high-Reynolds-number bubbles in inhomogeneous flows. *Annu. Rev. Fluid Mech.* **32** (1), 659–708.

MAGNAUDET, J. & MOUGIN, G. 2007 Wake instability of a fixed spheroidal bubble. *J. Fluid Mech.* **572**, 311–337.

MEI, R., KLAUSNER, J. F. & LAWRENCE, C. J. 1994 A note on the history force on a spherical bubble at finite Reynolds number. *Phys. Fluids* **6**, 418–420.

MERCIER, J., LYRIO, A. & FORSLUND, R. 1997 Three-dimensional study of the nonrectlinear trajectory of air bubbles rising in water. *Trans. ASME J. Fluids Engng* **119**, 233–247.

MOORE, D. W. 1965 The velocity of rise of distorted gas bubbles in a liquid of small viscosity. *J. Fluid Mech.* **23**, 749–766.

MOUGIN, G. & MAGNAUDET, J. 2001 Path instability of a rising bubble. *Phys. Rev. Lett.* **88** (1), 014502.

MOUGIN, G. & MAGNAUDET, J. 2002 The generalized kirchhoff equations and their application to the interaction between a rigid body and an arbitrary time-dependent viscous flow. *Intl J. Multiphase Flow* **28** (11), 1837–1851.

MOUGIN, G. & MAGNAUDET, J. 2006 Wake-induced forces and torques on a zigzagging/spiralling bubble. *J. Fluid Mech.* **567**, 185–194.

POSNER, A. M., ANDERSON, J. R. & ALEXANDER, A. E. 1952 The surface tension and surface potential of aqueous solutions of normal aliphatic alcohols. *J. Colloid Sci.* **7** (6), 623–644.

https://doi.org/10.1017/jfm.2013.571 Published online by Cambridge University Press

PROSPERETTI, A. 2004 Bubbles. *Phys. Fluids* **16**, 1852–1865.

PROSPERETTI, A., OHL, C. D., TIJINK, A., MOUGIN, G. & MAGNAUDET, J. 2003 The added mass of an expanding bubble. *J. Fluid Mech.* **482**, 286–290.

SADHAL, S. S. & JOHNSON, R. E. 1983 Stokes flow past bubbles and drops partially coated with thin films. Part 1. Stagnant cap of surfactant film–exact solution. *J. Fluid Mech.* **126** (1), 237–250.

SAFFMAN, P. G. 1956 On the motion of small spheroidal particles in a viscous liquid. *J. Fluid Mech.* **1**, 540–553.

SAFFMAN, P. G. 1992 *Vortex Dynamics*. Cambridge University Press.

SANADA, T., SUGIHARA, K., SHIROTA, M. & WATANABE, M. 2008 Motion and drag of a single bubble in super-purified water. *Fluid Dyn. Res.* **40** (7–8), 534–545.

SAVIC, P. 1953 Circulation and distortion of liquid drops falling through viscous medium. *Tech. Rep. MT-22. Natl Res. Counc. Can. Div. Mech. Engng*.

SHEW, W. & PINTON, J.-F. 2006 Dynamical model of bubble path instability. *Phys. Rev. Lett.* **97** (14), 144508.

SHEW, W. L., PONCETT, S. & PINTON, J.-F. 2006 Force measurements on rising bubbles. *J. Fluid Mech.* **569**, 51–60.

TAKAGI, S. & MATSUMOTO, Y. 2011 Surfactant effects on bubble motion and bubbly flows. *Annu. Rev. Fluid Mech.* **43** (1), 615–636.

TAKAGI, S., UDA, T., WATANABE, Y. & MATSUMOTO, Y. 2003 Behavior of a rising bubble in water with surfactant dissolution (1st report, steady behaviour) (in japanese). *Trans. JSME, Series* B **69**, 2192–2199.

TAKEMURA, F. & YABE, A. 1999 Rising speed and dissolution rate of a carbon dioxide bubble in slightly contaminated water. *J. Fluid Mech.* **378**, 319–334.

TOMIYAMA, A., CELATA, G. P., HOSOKAWA, S. & YOSHIDA, S. 2002 Terminal velocity of single bubbles in surface tension force dominant regime. *Intl J. Multiphase Flow* **28** (9), 1497–1519.

TSUGE, H. & HIBINO, S. 1971 The motion of single bubble gas bubbles in various liquids. In *Kagaku-kogaku*, pp. 65–71.

VELDHUIS, C., BIESHEUVEL, A. & VAN WIJNGAARDEN, L. 2008 Shape oscillations on bubbles rising in clean and in tap water. *Phys. Fluids* **20** (4), 040705.

DE VRIES, A. W. G., BIESHEUVEL, A. & VAN WIJNGAARDEN, L. 2002 Notes on the path and wake of a gas bubble rising in pure water. *Intl J. Multiphase Flow* **28** (11), 1823–1835.

WANG, Y., PAPAGEORGIOU, D. T. & MALDARELLI, C. 2002 Using surfactants to control the formation and size of wakes behind moving bubbles at order-one Reynolds numbers. *J. Fluid Mech.* **453**, 1–19.

WU, M. & GHARIB, M. 2002 Experimental studies on the shape and path of small air bubbles rising in clean water. *Phys. Fluids* **14**, L49.

YANG, B. & PROSPERETTI, A. 2007 Linear stability of the flow past a spheroidal bubble. *J. Fluid Mech.* **582**, 53–78.

ZENIT, R. & MAGNAUDET, J. 2008 Path instability of rising spheroidal air bubbles: A shape-controlled process. *Phys. Fluids* **20** (6), 061702.

ZENIT, R. & MAGNAUDET, J. 2009 Measurements of the streamwise vorticity in the wake of an oscillating bubble. *Intl J. Multiphase Flow* **35** (2), 195–203.

ZHANG, Y. & FINCH, J. A. 2001 A note on single bubble motion in surfactant solutions. *J. Fluid Mech.* **429**, 63–66.

https://doi.org/10.1017/jfm.2013.571 Published online by Cambridge University Press